The projected sensitivity of SCEP experiment to Magnetic Monopole

Changqing Ye,[1, 3, *] Beige Liu,[1, 3, *] Zhe Cao,[1, 2, 3, †] Lingzhi Han,[1, 3] Xinming Huang,[3, 4, 5, 6] Min Jiang,[3, 4, 5, 6, 2] Dong Liu,[2] Qing Lin,[1, 2, 3, ‡] Shitian Wan,[1, 3] Yusheng Wu,[1, 2, 3] Lei Zhao,[1, 2, 3, §] Yue Zhang,[1, 3] Xinhua Peng,[3, 4, 5, 6, 2, ¶] and Zhengguo Zhao[1, 2, 3, **]

(SCEP Collaboration)

[1] *State Key Laboratory of Particle Detection and Electronics, University of Science and Technology of China, Hefei 230026, China*

[2] *Deep Space Exploration Laboratory, Hefei, 230022, China*

[3] *Department of Modern Physics, University of Science and Technology of China, Hefei 230026, China*

[4] *Hefei National Laboratory for Physical Sciences at the Mcroscale, University of Science and Technology of China, Hefei, 230026, China*

[5] *CAS Key Laboratory of Microscale Magnetic Resonance, University of Science and Technology of China, Hefei, 230026, China*

[6] *Synergetic Innovation Center of Quantum Information and Quantum Physics, University of Science and Technology of China, Hefei, 230026, China*

(Dated: May 14, 2024)

The investigation of beyond-Standard-Model particles is a compelling direction in the pursuit of new physics. One such hypothetical particle, the magnetic monopole, has garnered considerable attention due to its strong theoretical motivation and potential to unveil profound physical phenomena. The magnetic monopole is intricately linked to the long-standing enigma surrounding the quantization of electric charge. In this manuscript, we propose a novel detection scenario for magnetic monopoles by employing a coincidence measurement technique that combines a room-temperature magnetometer with plastic scintillators. This setup allows for the collection of both the induction and scintillation signals generated by the passage of a monopole. The estimation of the sensitivity using a simple benchmark setup is given.

I. INTRODUCTION

The relentless pursuit of uncovering new physics occupies a prominent position in modern scientific exploration. Despite the remarkable success of the Standard Model (SM) of particle physics in elucidating the behavior of fundamental particles and their interactions, it is widely acknowledged that SM remains incomplete. Numerous enigmatic phenomena persist as tantalizing mysteries, including the elusive nature of dark matter, the perplexing origin of matter-antimatter asymmetry, and the unification of fundamental forces. Consequently, physicists actively engage in tireless searches for novel physics beyond the SM. This endeavor encompasses both theoretical advancements and experimental undertakings, propelling the boundaries of human comprehension and challenging existing scientific paradigms. Among the directions pursued in these explorations, the search for beyond-Standard-Model particles plays a pivotal role, compelling researchers to employ state-of-the-art detector techniques to scrutinize hypothetical particles that hold the potential to unveil the secrets of new physics. Magnetic monopole is one prominent candidates for beyond-Standard-Model particles that have garnered considerable attention within the scientific community.

A magnetic monopole (MM) is a theoretical particle postulated to exist as an isolated source of a singular magnetic charge, analogous to the individual positive or negative electric charges observed in particles. Proposed by Paul Dirac in 1931 [1] as a consequence of his pioneering work on the quantization of electric charge, MMs hold significance in fundamental physics as they provide a means to unify electromagnetism and explain the quantization of charge. The concept of MMs finds natural incorporation within the framework of Grand Unified Theories (GUTs) [2], which aim to unify the electromagnetic, weak, and strong nuclear forces. The quantization of electric charge is also explained in the framework of GUT. The search for MMs persists through various experimental approaches, prominently including ultra-low background experiments and superconducting coil-based experiments, which strive to detect the elusive presence of these MMs and further our understanding of the fundamental laws. Ultra-low background experiments are typically conducted in underground environments with kilometers of rock overburdens, providing shielding against cosmic rays. These experiments aim to detect the ionization or scintillation signals produced by MMs as they traverse the target material of the detector. Notably, the MACRO experiment [3], based on liquid scintillator

* These two authors contributed equally to this work.
† Corresponding author:caozhe@ustc.edu.cn
‡ Spokesperson & Corresponding author:qinglin@ustc.edu.cn
§ Corresponding author:zlei@ustc.edu.cn
¶ Corresponding author:xhpeng@ustc.edu.cn
** Corresponding author:zhaozg@ustc.edu.cn

technology, and the neutrino telescope IceCube [4] have yielded the most sensitive searches for MMs with speeds greater than 4×10^{-5} times the speed of light. While the ionization density caused by MMs is predicted to be significantly higher than that of background particles commonly observed in terrestrial detectors, such as muons and electrons, it is important to consider the possibility of alternative exotic particles, such as superheavy dark matter [5, 6], which could also contribute to high-density ionization. Conversely, superconducting coil-based experiments [7, 8] focus on detecting the smoking-gun induction signals generated by MMs. However, these experiments face limitations in terms of size due to the requirement of maintaining superconducting temperatures.

This article presents a comprehensive illustration of the SCEP (Search for Cosmic Exotic Particles) experiment, with a specific emphasis on the detection perspective of MMs. We propose a novel approach utilizing a coincidence measurement technique that combines room-temperature magnetometers with plastic scintillators (PS). The fundamental concept of the detector system is illustrated in Section II. To assess the capabilities of the proposed system, we have developed a sophisticated simulation framework, which is described in Section III. The validation of the simulation framework is performed and described in Section IV. Furthermore, the anticipated background and sensitivity of the SCEP experiment to MMs are presented in Section V.

II. DETECTOR CONCEPT

A single module of the SCEP detector encompasses dedicated detection systems for both the scintillation and induction signals, as illustrated in Fig. 1. The scintillation signals are captured by PSs positioned at the top and bottom of the module. In the preliminary design, each PS module is constructed using the designs similar to the ones utilized in previous works [9]. To guide the scintillation light, wavelength-shifting fibers are strategically incorporated within the PS module. These fibers serve the purpose of directing the emitted light to Silicon photomultipliers (SiPMs) coupled at the ends of the fibers. A preliminary simulation using the GEANT4 toolkit [10] has been conducted to evaluate the performance of the PS module. The obtained results indicate a light yield of approximately 22 photoelectrons (PE) per MeV, thereby enabling an energy resolution of about 8.6% and 2.5% for muons at $\sim$8 MeV and Dirac MMs at $\sim$ 100 MeV, respectively.

The induction signals resulting from the passing through of a MM are collected using a specialized apparatus that integrates an induction coil, a Helmholtz coil, and a magnetometer. The micro-current induced by the MM passing through the induction coil is subsequently directed to the Helmholtz coil, leading to the generation of an alternating magnetic field

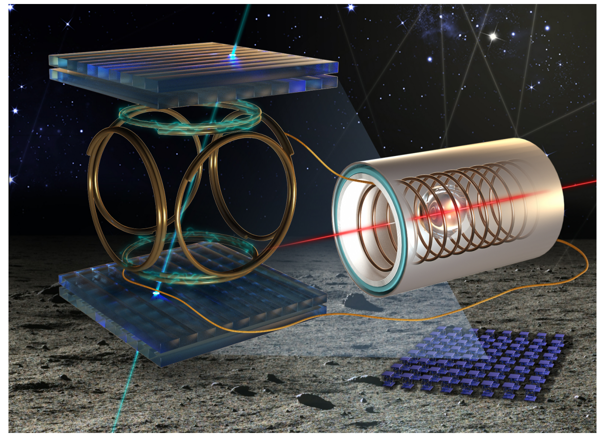

FIG. 1. Schematic diagram of single module detector of SCEP.

at the center of the Helmholtz coil. Subsequently, the alternating magnetic field is detected utilizing a magnetometer renowned for its exceptional sensitivity [11, 12]. This magnetometer is meticulously designed to exhibit an extraordinary level of sensitivity towards the variations in magnetic fields. The target material of the magnetometer is confined in a transparent gas chamber, and is polarized by the static magnetic field aligned along the Z axis with the assistance of a beam of bump laser. The presence of an alternating magnetic field in the XY plane can impact the precession of the atoms within the gas chamber. This effect manifests as the variations in the light density of a laser beam which pass through the gas chamber. More details of the magnetometer are given in Ref. [12]. A preliminary prototype of the magnetometer can reach a detection sensitivity of $1\,\mathrm{fT}/\sqrt{\mathrm{Hz}}$ for the alternating magnetic field []. Besides, an alternative readout scenario is being considered for the search of high-speed MM. This scenario involves a direct connection between the induction coil, an operational amplifier (OPA), and an analog-to-digital converter (ADC). Although this setup exhibits higher intrinsic noise levels compared to the use of a magnetometer as the readout method, it provides the benefits of quicker response times, compact size conducive to integration, and more cost-effective, lightweight systems.

III. SIMULATION OF SIGNAL

The signal-to-noise ratio (SNR) to Dirac MM stands as a critical parameter governing the quality of the induction signal. The SNR in this work is defined as the maximum signal amplitude squared A_S^2 divided by the mean-squared noise amplitude $\langle A_N^2\rangle$:

$$\mathrm{SNR} = \frac{\mathrm{MAX}(A_S^2)}{\langle A_N^2\rangle}. \quad (2)$$

$$U = -\frac{g_m n}{2\pi} \frac{(z_N^2 + (1-\rho_N)^2)(z_N\rho_T - \rho_N z_T)\mathcal{K}\left(\frac{4\rho_N}{z_N^2+(1+\rho_N)^2}\right) + (z_T\rho_N(\rho_N^2 + z_N^2 - 1) - z_N(1 + z_N^2 + \rho_N^2)\rho_T)\mathcal{E}\left(\frac{4\rho_N}{z_N^2+(1+\rho_N)^2}\right)}{(z_N^2 + (1-\rho_N)^2)\rho_N\sqrt{z_N^2 + (1+\rho_N)^2}},$$

$$\text{with} \begin{cases} \rho_N = \sqrt{(v_N t \sin\theta)^2 + (\rho_0/R)^2 + 2v_N t(\rho_0/R)\sin\theta\cos\phi} \\ \rho_T = (v_N(\rho_0/R)\cos\phi\sin\theta + v_N^2 t\sin^2\theta)/\rho_N \\ z_N = v_N t\cos\theta \\ z_T = v_N\cos\theta \\ v_N = v/R \end{cases} \tag{1}$$

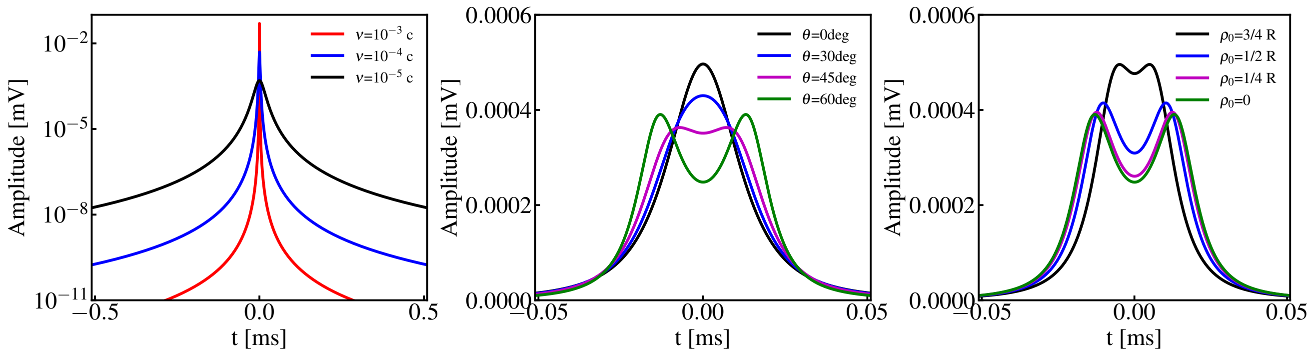

FIG. 2. Simulated waveforms for the induction voltages by MMs. The left, middle, and right panels shows the induction signals with different MM velocities, polar angles, and azimuth angles, respectively. The waveforms in the middel and right panels are calculated assuming ν=10^{-5}c. These waveforms are calculated assuming an induction coil with 12-cm diamater and about 4320 turns.

Larger values of SNR are preferred for higher noise rejection power. This criterion allows for the utilization of a lower number of coil coincidences in detector array while still attaining a relatively high level of noise rejection. The SNR of the system is related to various factors, including the electrical parameters encompassing the circuitry from the induction coil to the Helmholtz coil, the prevailing temperature conditions, the signal response characteristics of the magnetometer, and other relevant factors. These factors collectively contribute to the overall SNR, influencing the system's ability to discern and extract the desired signal amidst the presence of noise. To estimate the SNRs for MMs with various velocities and to optimize the design of the induction system, a comprehensive simulation framework has been developed which is described briefly in the following subsections. It should be noted that in this manuscript, the magnetic charge of Dirac MM is employed as a reference standard for the calculation of scintillation and induction signals attributed to a MM.

A. Induction

The induction voltage on the induction coil is calculated assuming that the thickness of coil brings negligible effect. When a MM with velocity of v passing through the induction coil with radius of R, the induction voltage U can be written as in Eq. 1. Eq. 1 is based on the assumption that the time t is 0 when the MM reaches the coil plane ($z = 0$). ρ_0 is the transverse distance to the coil center when the MM reaches the coil plane. θ and ϕ represent the polar angle and azimuth angle, respectively, of the incoming MM's direction under the spherical coordinates with the z axis perpendicular to the coil plane. The $g_m = 4.14125 \times 10^{-15}$ Wb is the magnetic charge of Dirac MM [1], and n is the coil turn number. The $\mathcal{K}$ and $\mathcal{E}$ functions are the complete elliptic integrals of the first and second kinds, respectively. The induction signal is at maximal when the MM passes through the coil center with $\theta = 0$. The amplitude and spectral shape of the induction signals are predominantly influenced by the MM speed, the polar angle, and the azimuth angle. These dependencies are visually depicted in Fig. 2.

The interaction of charged SM particles or SM particles with magnetic moments with the induction coils can potentially result in induction signals. However, there are significant distinctions in the amplitude and spectral shape of these signals compared to those induced by the MMs. More importantly, the induction signals generated by SM particles have a vanishing time integral due to their nature as, at most, magnetic dipoles. On the other hand, common background SM particles, such as muons, neutrons, and protons, typically exhibit relativistic speeds, leading to rapid resonant induction on the timescale of approximately 10 picoseconds for a

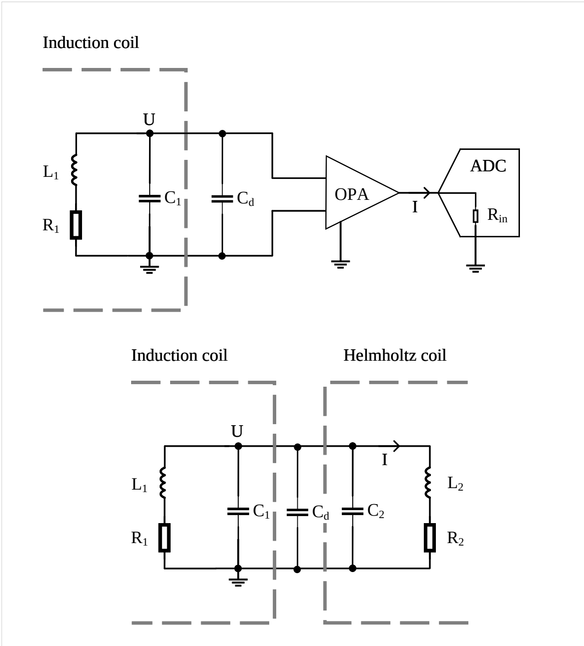

FIG. 3. Circuit diagrams for the ADC readout (top) and magnetometer readout scenarios.

coil with a 12-centimeter diameter. The quick oscillation of voltage cannot be effectively shaped by subsequent relatively slow circuitry or reliably detected by read-out devices. Considering these factors, the induction caused by SM particles is considered to be negligible in practical scenarios.

B. Signal shaping

The induction coil and the Helmholtz coil are connected in series[13]. These coils possess non-trivial resistances, capacitances, and inductances, which affect both the amplitude and temporal characteristics of the electric current within the circuit. In the signal simulation, it is assumed that the coil can be approximated as a series combination of a resistor and an inductor, paralleled by a capacitor. The circuit diagram of the induction and Helmholtz coils in the magnetometer-readout scenario, as well as of the direct read-out scenario using the ADC, is depicted in Fig. 3. In the circuit diagram, L_1 (L_2), R_1 (R_2), and C_1 (C_2) are the effective inductance, resistance, and capacitance, respectively, of the induction (Helmholtz) coil. C_d represents other parallel capacitive components in the circuit, mainly the distributed capacitance of the cable and the input capacitance of the OPA. U is the induction voltage, and I is the induction current on the Helmholtz coil which is directly related the strength of magnetic field that is eventually captured by the magnetometer in magnetometer-readout scenario. In the alternative ADC-readout scenario, I denotes the flow of electric current into the ADC.

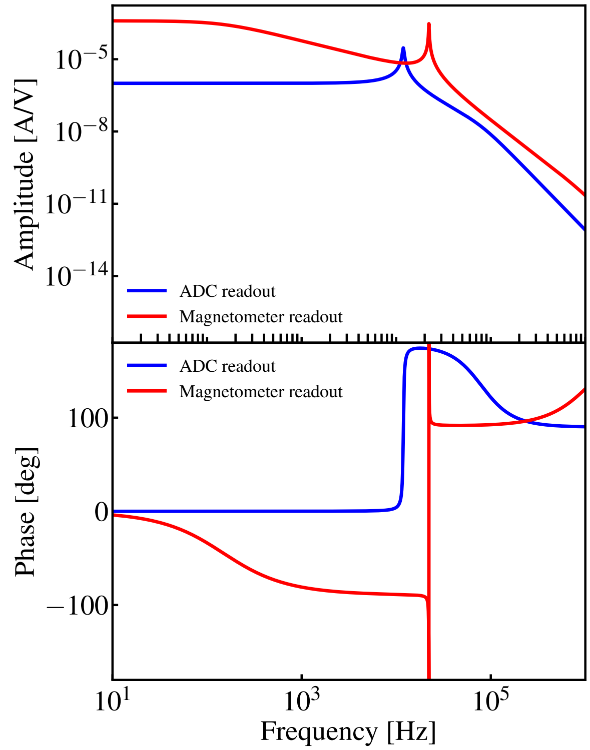

FIG. 4. Response functions of the circuits with different readout scenarios. The top and bottom panels show the amplitude and phase spectra, respectively. The red and blue lines represent the ADC and magnetometer readout scenarios.

In the context of signal simulation framework, the electric current I is determined by applying a circuit response function to the induction voltage U. The Fourier transform of the electric current, denoted as $i(\omega)$, can be expressed as:

$$i(\omega) = u(\omega) \cdot \mathcal{H}(\omega) \tag{3}$$

where the complex $u(\omega)$ is the Fourier transform of the induction voltage. The circuit response function $\mathcal{H}(\omega)$ is analytically derived based on the effective circuit models shown in Fig. 3. A response function for a 6-cm-radius coil with 4320 turns is presented in Fig. 4. The resonant frequencies of the two readout scenarios exhibit variations owing to disparities in the circuit configurations. In particular, the inductance L_2 and capacitance C_2 of the Helmholtz coil in the magnetometer readout scenario contribute to a higher resonant frequency compared to the alternative ADC readout scenario. Among the various electric parameters, the resistance of the induction coil R_1 is identified as the most dominant factor. The resistance depends on the signal frequency ω, mainly due to the presence of the skin effect and the proximity effect. However, the exact relation between the coil resistance and signal frequency cannot be analytically given due to the complexity of the coil structure. To investigate the frequency

Coil	Wire type	Wire diameter [mm]	Minimal coil radius [cm]	Maximal coil radius [cm]	Turn number	Optimized SNR_0	
						ADC readout	Mag. readout
V1	Simple	0.11	5.7	7.2	4320	0.16	0.16
V2	Litz	1.35	5.7	7.2	720	0.02	1.92
V3	Simple	0.55	10.0	14.5	12500	0.57	0.82

TABLE I. The geometrical parameters and best SNRs to single Dirac MM for the benchmark induction coils. The SNRs listed are based on the assumption that MM's velocity is 10^{-5} light speed, and the MM perpendicularly crosses the coil center.

dependence of the coil resistance, *in-situ* measurements are conducted using an LCR meter. The LCR meter is connected in parallel to the induction coil to measure the magnitude, denoted as Z_c, and the phase angle, denoted as θ_c, of the complex impedance of the coil. The Z_c and θ_c have correlation with the inductance L, capacitance C, and resistance R_{AC} of the coil, which can be expressed as:

$$Z_c = \sqrt{\frac{{R_{AC}}^2 + \omega^2 L^2}{1 - 2\omega^2 LC + \omega^2 C^2 (R_{AC}^2 + \omega^2 L^2)}}$$
$$\theta_c = \frac{\omega (L - C{R_{AC}}^2 - \omega^2 L^2 C)}{R_{AC}}. \tag{4}$$

The alternating resistance of the induction coil R_{AC} is empirically parameterized as [14]:

$$R_{AC}(\omega) = \alpha\omega^{\beta} + R_{DC}, \tag{5}$$

where R_{DC} is the direct resistance of the coil, which is independent of signal frequency. The parameters α and β are empirical model parameters. Once the complex impedance of the coil is measured including Z_c and θ_c, a Nelder-Mead fitting algorithm is utilized to derive the resistance of the coil. In the benchmark tests, three induction coils with different radius and turn numbers are manufactured and tested. Their geometrical parameters are given in Table I. The measured R_{AC} results for these induction coils are shown in Fig. 5. The waveforms of the induction electric current on the Helmholtz coil in magnetometer readout scenario and of electric current flowing into ADC in alternative readout scenario (the current I in Fig. 3) are shown in Fig. 6, assuming the MM perpendicularly pass the induction coil center.

C. Detection

The readout devices exhibit diverse response characteristics to induction signals, owing to their distinct intrinsic mechanisms. The magnetometer relies on atomic precession and typically demonstrates a response timescale ranging from several tens of microseconds to milliseconds. The complex response function of the magnetometer $\mathcal{H}_m$ is commonly modeled in the form of a Lorentzian distribution:

$$\mathcal{H}_m(\omega) = \frac{\gamma T_2}{2j + 2T_2(\omega_0 - \omega)}, \tag{6}$$

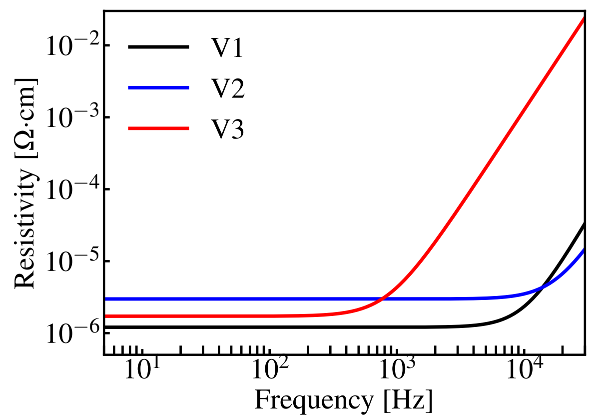

FIG. 5. Measured frequency-dependent resistivities as a function of signal frequency for the benchmark induction coils.

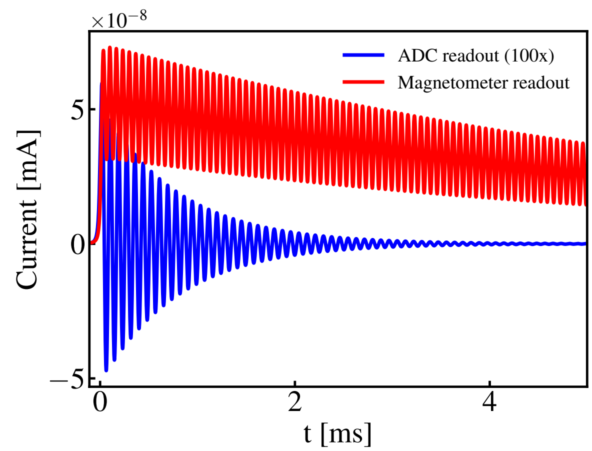

FIG. 6. The waveforms of the electric currents after the circuit shaping. The red and green solid lines represent the scenarios of the magnetometer and ADC readout, respectively. To increase the visibility, the current from ADC readout is amplified by 100 times.

where $\gamma = \frac{2\mu_B}{5\hbar}$, with μ_B the Bohr magnetic moment and $\hbar$ reduced Planck constant, is gyromagnetic ratio of atom caesium and T_2 is the spin relaxation time which can be measured experimentally. The mean resonant frequency ω_0 of the Lorentzian response function of the magnetometer varies depending on the applied static magnetic field along the z axis within the gas chamber. In the case of using an ADC for readout, the response function can be simplified and approximated as

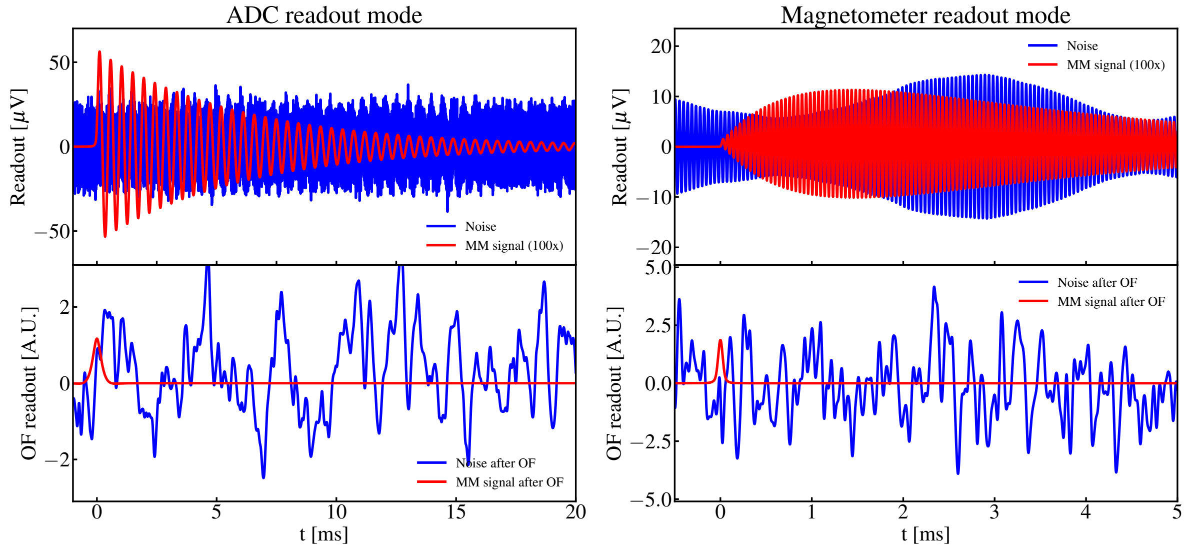

FIG. 7. The waveforms of readout signals for the ADC and magnetometer readout scenarios are displayed in the left and right panels, respectively. The top and bottom panels show the waveforms before and after OF applied. The V3 and V2 coils are used for the ADC- and magnetometer-readout scenarios, respectively, having an average SNR_0 to the MM of 0.57 and 1.92. The red and blue solid lines correspond to the waveforms of MM signal and noise. To enhance visibility, the MM signal waveforms before the OF applied are scaled by 100 times.

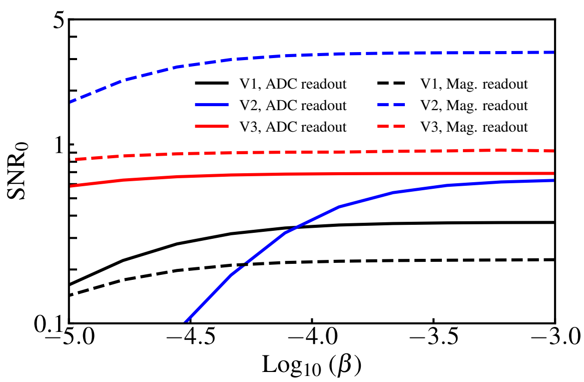

FIG. 8. The SNR_0 as a function of MM speed for the prototype induction coils for the ADC-readout and magnetometer-readout modes.

a constant which is dependent on the gain of the OPA and the input impedance of the ADC, within the bandwidth of interest.

D. Reconstruction and thermal noise

To extract the MM signals from a significant amount of noise, the readout output undergoes signal filtering to obtain the final signals. In our case, the optimal filter (OF) method is applied for signal extraction. The response function of OF, denoted as $\mathcal{H}_{\mathrm{OF}}$, can be written as [14]:

$$\mathcal{H}_{\mathrm{OF}} = \frac{u^*(\omega)}{S_n(\omega)\prod \mathcal{H}_i^*(\omega) + S_H(\omega)}, \tag{7}$$

where S_n is the power spectral density of the noise on the induction coil. S_H is the power spectral density of the noise generated during the signal shaping and detection, while $\prod \mathcal{H}_i^*(\omega)$ represents the product of the conjugates of all response functions present in the same progress. In the ADC-readout scenario, $\prod \mathcal{H}_i^*(\omega)$ corresponds to the conjugate of the circuit response function $\mathcal{H}^*$, and the S_H is mainly influenced by the noise from the OPA. On the other hand, in the magnetometer-readout scenario, $\prod \mathcal{H}_i^*(\omega)$ represents the combined conjugate response of both the circuit and magnetometer $\mathcal{H}^*\mathcal{H}_m^*$, and S_H accounts mainly for the thermal noise from the Helmholtz coil. The noise from the magnetometer is negligible. Thermal noise originating from the induction coil significantly influences the overall noise characteristics, especially in the magnetometer-readout scenario. This noise is modeled as Johnson-Nyquist noise [15] [16]:

$$S_n(\omega) = 4k_B T R_{AC}(\omega), \tag{8}$$

where k_B is the Boltzman constant, and T is the temperature. It is essential to emphasize that the thermal noise in this particular scenario does not exhibit the characteristic of "white" noise, which is typically assumed to have a frequency-independent power spectral density. Due to the presence of a non-trivial alternating resistance in the induction coil, the thermal noise power increases with higher frequencies. This frequency-dependent behavior of the noise is an important consideration in the analysis and characterization of the system. In order to reduce spectral waveform distortions due to limited-length time window, specific-shaped time windows, such as the Hamming window [17], are introduced in signal and noise processing. Fig. 7 shows some waveform examples before and after applying OF for both the ADC-readout and magnetometer-readout scenarios.

The typical SNR is calculated under the assumption of MM velocity being 10^{-5} light speed, passes perpendicularly through the coil center(denoted as SNR_0 in the text). The SNR_0s of each prototype coil can be found in Tab. I. It is worth noticing that the SNR_0 does depend on the MM's speed. SNR_0 increases with the increase in MM speed. However, SNR_0 gradually tends toward saturation as the effect of alternating resistance increasingly becomes significant. Fig. 8 displays the SNR_0 of the prototype induction coils in both ADC-readout and magnetometer-readout modes.

IV. VALIDATION OF THE SIGNAL SIMULATION

A validation test is performed to assess the accuracy and reliability of the signal simulation framework. The test mainly aims to validate the waveform amplitudes and shapes of MM signal and noise. These characteristics of the signal waveforms are crucial for predicting the sensitivity of such detection to single Dirac MM.

A. Signal validation

The MM signal validation involves the utilization of a long-thin stimulation coil to generate a pulsed magnetic field that emulates an MM signal on the manufactured induction coil prototypes. Table I shows the geometrical parameters of the induction coils, including the wire type, wire diameter, coil minimal/maximal radii, and turn number. Their alternating resistivities are displayed in Fig. 5. The corresponding SNR_0s to single Dirac MM are given in Table I as well. The highest SNR with ADC readout is about 0.57, mainly limited by the thermal noise of the induction coil and the noise of OPA. On the contrary, the highest SNR_0 with magnetometer readout can reach 1.92 because of the low noise level of the magnetometer. However, the parameters of the Helmholtz coils need to be carefully designed. The stimulation coil utilized in the validation has a length of 50 cm and a diameter of 10 mm. The turns number density amounts to approximately 100 per centimeter. During the testing, the stimulation coil passes through the center of the induction coil, perpendicular to its coil plane. The diagram of the induction coil, the stimulation coil, and their positioning are shown in Fig. 9.

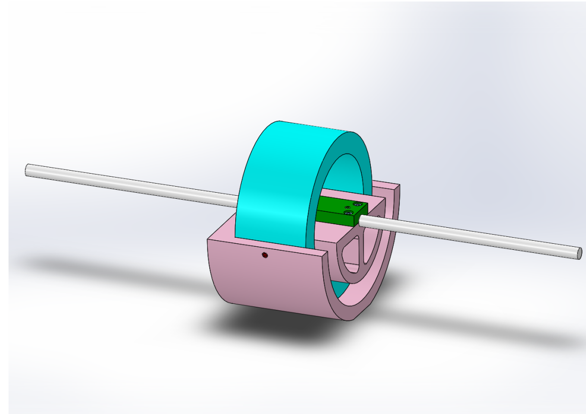

FIG. 9. Diagram of the testing apparatus for signal validation. The white and cyan parts are the stimulation and induction coils, respectively. The pink and green parts are the supporting PTFE structure.

Due to the prevalence of electromagnetic noise in the surrounding environment and the limited precision of the pulse generator, it is not practically feasible to accurately simulate and test the signal response of the induction coil to a single Dirac MM. In our experimental setup, we generate a voltage pulse with a square wave shape using a pulse generator, and then feed this voltage pulse to the stimulation coil. A resistor with a resistance of 19.36 Ω is connected in series with the stimulation coil. The voltage drop across this resistor is monitored using a digitizer with a sampling rate of 2 MHz, which is connected in parallel to the resistor. This allows us to precisely model the microcurrent passing through the stimulation coil. It should be noted that in our experimental setup, we assume there are no leak fields associated with the tightly wound stimulation coil. By employing this stimulation process, we are able to generate magnetic flux pulses on the induction coil that closely mimic those produced by the passing of MM in temporal shape.

Such test is performed for all three prototype induction coils with the ADC-readout scenario. For the magnetometer-readout scenario, V2 coil is tested which is expected to have the largest SNR among all three prototype coils. Fig. 10 shows the comparison between the measured and predicted test signals in the time domain. The readout signals can be parameterized as:

$$S(t) = A\sin(\omega t + \phi) \cdot e^{-t/\delta}, \tag{9}$$

where ϕ is the phase. The A, ω, and δ are the amplitude, frequency, and delay rate, respectively. These three parameters are compared between the expectation and measurement. The results of the comparison are summarized in Table II. The measured frequencies and decay rates are consistent with the predictions, with bias no more than 0.3% and 8.7% for the frequency and decay rate, respectively. This validates our response function models of the circuit and magnetometer. The largest amplitude differences observed between measurements and predictions are about 12.5% for ADC readout and

9.2% for magnetometer readout. This is considered to be due to the leak fields and non-even turn density of the stimulation coil. Particularly the field leakage is more severe since the size of V3 coil is the largest among the tested ones. In addition, the lower amplitude seen in the measurement with magnetometer readout could be due to the potential bias of the effective Lorentzian response shown in Eq. 6.

Coil	ADC readout			Mag. readout
	V1	V2	V3	V2
A_{msr}/A_{prd}	0.973	1.041	0.875	0.908
ω_{msr} [kHz]	58.8	296.5	2.0	61.4
ω_{prd} [kHz]	58.9	297.1	2.0	61.4
$\omega_{msr}/\omega_{prd}$	0.999	0.998	1.003	0.999
δ_{msr} [ms]	1.058	0.703	10.309	0.863
δ_{prd} [ms]	1.077	0.770	10.886	0.874
$\delta_{msr}/\delta_{prd}$	0.983	0.913	0.947	0.987

TABLE II. The ratios of the measured parameters versus the predicted ones. The parameters include the amplitude A, the resonant frequency ω, and the decay rate δ. The comparisons are performed for all three benchmark induction coils (V1, V2, and V3) with the ADC-readout scenario. The results of V2 test with the magnetometer-readout scenario are shown.

B. Noise validation

To determine the intrinsic thermal noise power spectrum, the V2 coil is enclosed within a grounded metal box constructed of copper, which served as a Faraday cage. Fig. 11 displays the power spectra of the V2 coil under two conditions: when the coil is exposed to air and when it is sealed inside the copper box. A significant reduction in noise is observed when the coil is enclosed in the copper box, indicating the presence of a strong electromagnetic noise background in the air. Furthermore, the frequency domain analysis revealed distinct peak-like structures upon placing the coil inside the copper box. These peaks corresponded to multiples of the common frequency in utility, suggesting the presence of leaked-in electromagnetic waves within the copper box, likely originating from the signal connectors. This hypothesis is supported by the observation that the orientation of the induction coil influences the level of noise detected. The lowest noise level is observed when the coil axis is in a vertical position, as shown in Fig. 11. The observed noise frequency spectrum closely resembled the predicted one by the simulation, with a slightly lower amplitude (8.0%) at the resonant frequency.

V. PROJECTED SENSITIVITY TO MAGNETIC MONOPOLE

The search for MMs eventually will be conducted using an array of induction coils. The top and bottom of the coil array are equipped with plastic scintillators, as depicted in Fig. 1. The experimental setup can be situated either on Earth or in deep space, such as on the Moon. In both scenarios, the detector array will be exposed to significant levels of background particles, specifically protons, muons, and alpha particles (helium nuclei). These background particles leave scintillation signals in the scintillators and can accidentally pile-up with the thermal noise in the induction coils, creating false MM signals. The impact of this background can be mitigated by requiring more layers of the induction coils and the particle detectors.

To assess the sensitivity of the detector array to MMs, we employ a simple ideal benchmark configuration. This configuration consists of induction coils with a diameter of 12 cm (same as V2 coil), arranged vertically and compactly instrumented. The array's size is assumed to be sufficiently large to disregard any edge effects. The alternating resistance (equivalent to the thermal noise configuration) of each induction coil is assumed to followed the one of V2 coil, and each coil is assumed to have negligible height. In this benchmark analysis, a simple over-threshold trigger is conducted on waveform of each induction coil after the OF applied. The coil array is equipped with PS layers at the top and bottom, and these layers are positioned approximately 1 meter apart in the benchmark. Each PS layer is composed of two sets of PS panels arranged perpendicular to each other. This arrangement allows for the reconstruction of events' transverse positions.

A. Acceptance to GUT-MM induction

The GUT-MM is assumed to exhibit isotropic behavior in terrestrial and deep-space environments. However, due to the round geometry of the induction coil, there is an inherent acceptance loss of (1-$\pi/4$) for each layer of coils. We consider simply the coil layers are identical and sufficiently close to each other, so that we can consider such benchmark setup having a conservative acceptance loss of (1-$\pi/4$) due to coil geometry. Optimizing the coil geometry and arrangement between layers can alleviate the acceptance loss to some extent.

The dependence of the SNR on the point of MM transpassing the coil is weak. In the upper panel of Fig. 12, the average acceptance to GUT-MM is displayed as a function of the transverse angle (θ), considering various assumptions regarding the SNR_0. Only when the θ approaches $\pi/2$, the acceptance drops quickly. The lower panel of Fig. 12 shows the angle-averaged acceptance as a function of SNR_0. All calculations are based on an MM speed of 10^{-5} times the speed of light.

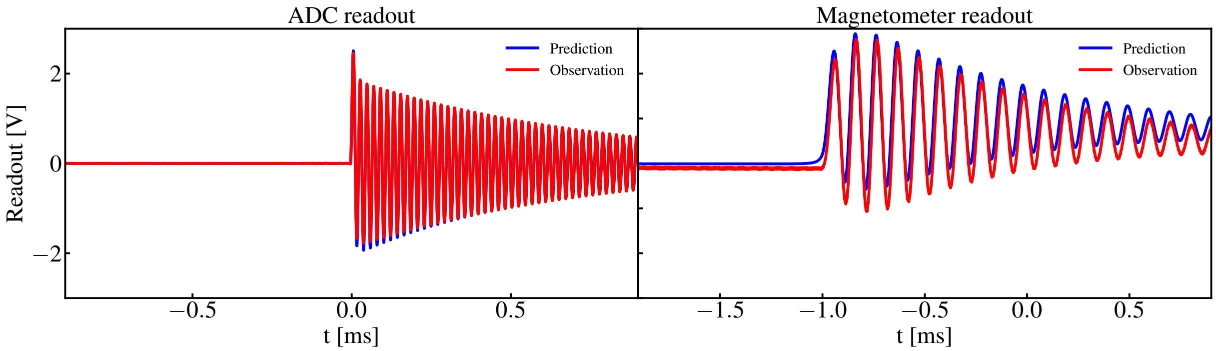

FIG. 10. The measured and predicted signal waveforms are shown in red and blue solid lines, respectively. The left panel shows the results for ADC readout scenario, and the right panel shows for the magnetometer readout scenario.

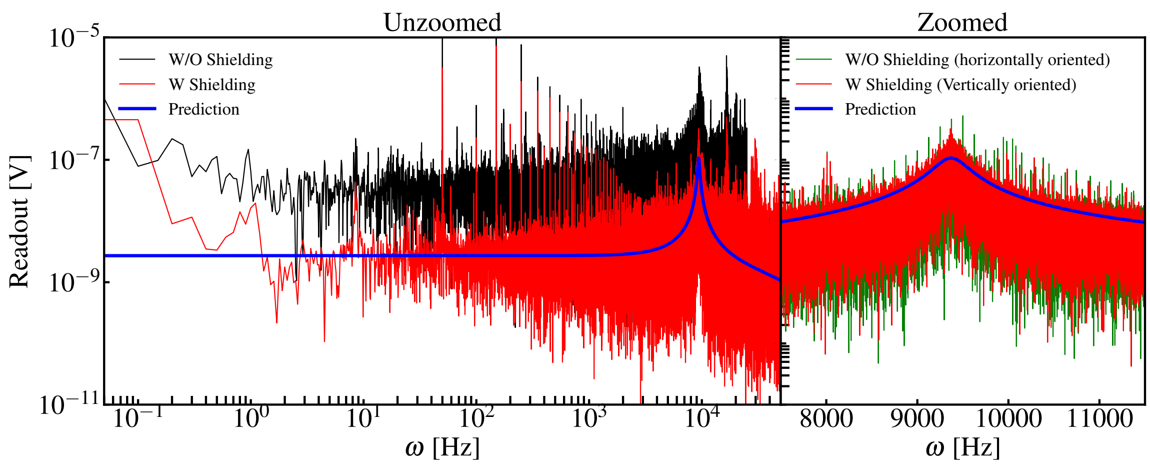

FIG. 11. The noise spectra with different setups. The left panel shows the unzoomed spectra with and without copper box as the electromagnetic shielding, in black and red solid lines, respectively. The blue solid line gives the predicted thermal noise spectrum. The right panel gives a zoomed view of the spectra with shielding, around the resonant frequency of the induction coil. The green solid line represents the noise spectrum when the induction coil is arranged so that its axis is oriented horizontally.

B. Background of Induction Signal

The cosmic rays and their secondaries, such as high-energy protons, muons, and electrons, that are common in terrestrial and deep-space environments, deposit energy in the top and bottom PSs, but produce negligible induction signals. These particles possess magnetic dipoles and travel mostly at relativistic speeds, resulting in a distinct induction pulse shape with a resonant shape and faster time response compared to those from the MMs. Therefore, we consider that relativistic cosmic rays and their secondaries do not produce any significant direct background in the induction signals.

However, the energy depositions detected by the PSs may coincide with the abundant thermal noise present in the induction coils, leading to mis-identified MM signals. As discussed in Subsection III D, the thermal noise arises from the non-zero alternating resistances of the induction coil and constitutes the main background for the MM induction signal search. When employing a simple over-threshold approach to trigger, for a single coil,the relationship of acceptance and noise rate with threshold(denote as α in the following article) at different SNR_0 are shown in the FIG.12. [(to be delete by Beige)Using the V2 induction coil as a benchmark, the estimated false-trigger rate due to thermal noise is approximately 6.8 Hz at room temperatures when employing a simple over-threshold approach on a single coil.] The rate of coincidental false triggering of thermal noise and the acceptance across the coils to form a track-like event can be expressed as follows:

$$\begin{cases} R_{ind}(\alpha) = \dfrac{(R_n(\alpha)\Delta t)^{N_c-1}}{N_c!} \cdot R_n(\alpha) \\ A_{ind}(\alpha) = A_n(\alpha)^{N_c} \end{cases} \tag{10}$$

Here, $R_n(\alpha)$ and $A_n(\alpha)$ represent the falsely triggered noise rate and acceptance of a single induction coil at a

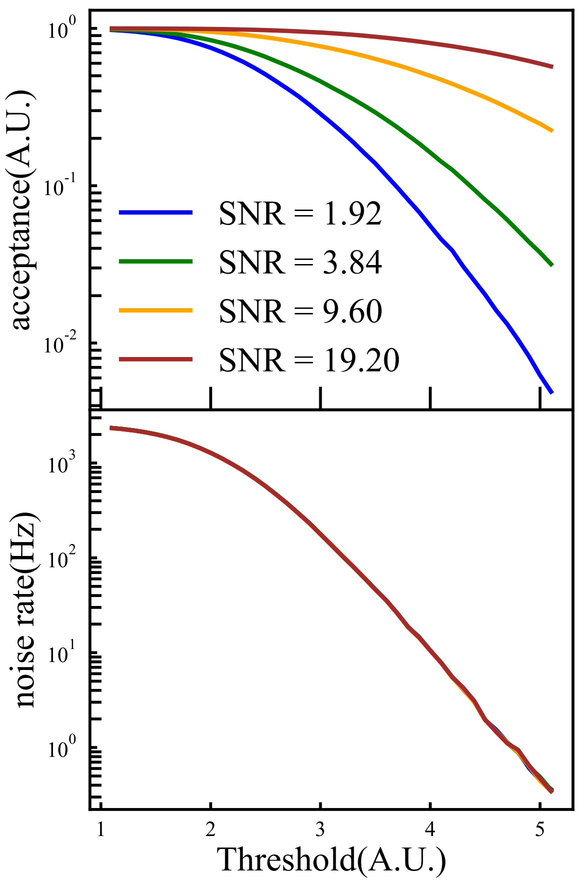

FIG. 12. Simulated coil's acceptance and thermal noise rate as a function of triggering threshold at different SNR_0 level

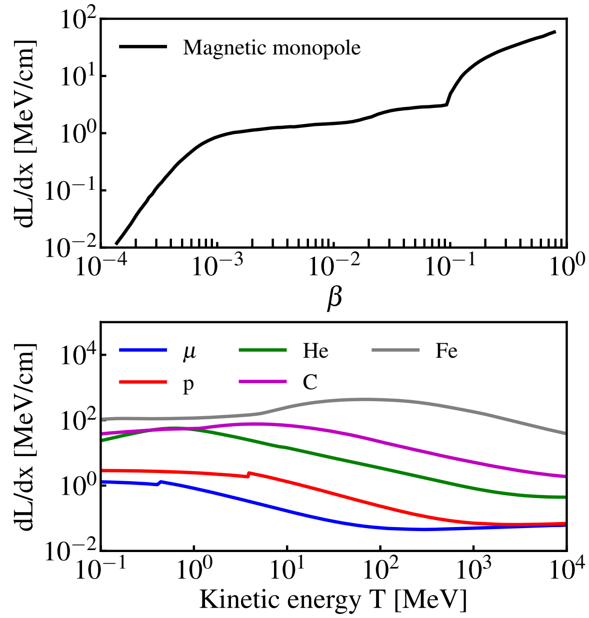

FIG. 13. The stopping power (detectable energies, or called light yield in the literature) dL/dx of a Dirac MM in plastic scintillator as a function of MM speed, based on [18], is shown in the upper panel. The dL/dx of the muon, proton, helium, carbon, and iron nucleus are shown in the lower panel. The dL/dx of muon is calculated based on the stopping power dE/dx from PDG [19]. The dE/dx of proton, helium, carbon, and iron nucleus are from PSTAR and ASTAR database [20].

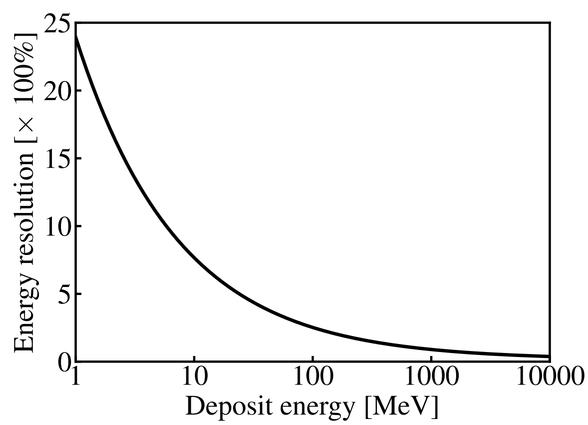

FIG. 14. The energy resolution as a function of total deposit energy of the plastic scintillator.

given threshold, N_c denotes the number of coils required to detect the induction trigger (coincidence number), and Δt represents the time response of the induction signal, which is related to the resonant frequency of the induction coil. For the benchmark analysis, we assume $\Delta t = 100\,\mu s$.

C. Background with Particle Coincidence

The rate of reconstructed scintillation signals on PSs is mainly affected by two factors: random pileups occurring between the top and bottom PSs, and the passage of a relativistic particle through both PSs. This reconstructed scintillation signal necessitates the presence of two energy depositions, one on each of the top and bottom PSs. It is crucial for the reconstructed energies, timings, and transverse positions of these two energy depositions to align with the expected energy, ToF, and track characteristics of the MM of interest. The differential reconstructed scintillation signal rate per unit area per radian on the two PS panels, represented as $\mathcal{R}_{PS}$, can be expressed as the sum of two components: the rate arising from pileup events, denoted as $\mathcal{R}_{pile}$, and the rate resulting from direct passage of particles, denoted as $\mathcal{R}_{part}$. Both contributions are related to the effective scintillation rate on a single PS given a zenith

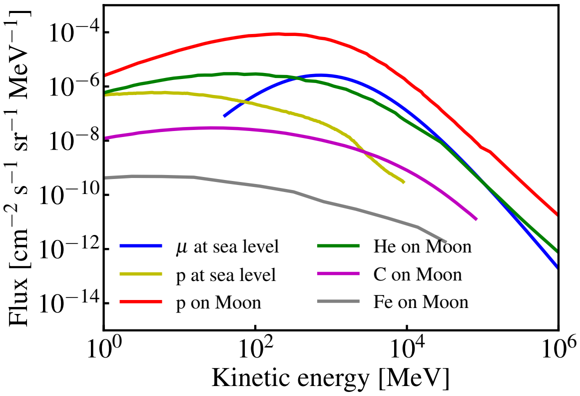

FIG. 15. The fluxes of background particles as a function of their kinetic energies. The blue and yellow solid lines represent the muon and proton fluxes at sea level, which are calculated based on Bugaev/Reyna model [21] and simulated by CRY algorithm [22], respectively. The red, green, magenta, and gray lines give the fluxes of proton, helium, carbon, and iron in space, taken from Ref. [23].

angle, denoted as $\mathcal{R}_{ion}(\theta)$ in unit of cm^{-2}s^{-1}sr^{-1}:

$$\begin{cases} \mathcal{R}_{pile}(\theta) = \frac{1}{2}\left(\int \mathcal{R}_{ion}(\theta')sin(\theta')d\theta'\right)^2 \Delta t_{PS}\frac{4\pi^3 d^2}{cos^3\theta}, \\ \mathcal{R}_{part}(\theta) = \int \epsilon^2(E)\mathcal{F}dE, \\ \mathcal{R}_{ion}(\theta) = \int \epsilon(E)\mathcal{F}dE, \end{cases} \tag{11}$$

where Δt_{PS} the pileup time window determined by the PS time resolution, which is assumed to be 10 ns [9], and d=1 m is the distance between top and bottom PSs. We require $\mathcal{R}_{ion}$ to be the rate after an energy range cut that covers 99.5% (3σ) of MMs and Such cuts gives an effective efficiency to background particles of $\epsilon(E)$. The $\mathcal{F}$ is the particle flux. Note that for different assumed speed of MMs, $\epsilon(E)$ is different. The total background rate that taken all the angles into account can be expressed as:

$$R_{ps}(\beta) = 2\pi \int (\mathcal{R}(\theta)_{pileup} + \mathcal{R}(\theta)_{part})sin(\theta)d\theta\cdot \tag{12}$$

In practice, the value of R_{ion} is influenced by several factors, including the background particle flux and spectrum, the ability to determine the direction of the MM using induction signals on the coils, and the energy resolution of the PS. The amount of light produced in the PS by Dirac MM depends on the MM velocity. The detectable stopping power, also known as the light yield, of Dirac MM on the PS as a function of MM speed is presented in the top panel of Fig. 13, based on the calculations in Ref. [18]. To differentiate the energy deposition of the MM from common background particles such as protons, electrons, alpha particles, and muons, we require that the reconstructed energy falls within 3 times the energy resolution. The intrinsic energy resolution of the PS, as a function of the total deposited energy, is obtained through optical simulation using GEANT4 [10]. The energy resolution is illustrated in Fig.14. The reconstruction resolution of the transverse position in the PS-based array primarily depends on the width of the PS panel, which is significantly smaller than the size of the induction coil. Consequently, the track reconstructed by the PS exhibits much higher resolution compared to the one reconstructed by the induction coils. For this benchmark analysis, we conservatively consider $\mathcal{R}_{pile}$ after the coincidence requirement to be the background rate within a 12 cm-diameter circle, which corresponds to the size of the V2 coil used in the estimation.

In a terrestrial detector situated at sea level, the primary background particles are atmospheric muons, which are generated when high-energy protons (cosmic rays) collide with the Earth's atmosphere, as well as the residual high-energy protons. Muons with kinetic energies ranging from hundreds of MeV to hundreds of GeV exhibit minimal ionizing behavior when interacting with matter, enabling them to easily traverse the surrounding materials near the detector, including the top and bottom PSs. On the other hand, the proton flux experiences a significant reduction as it traverses the atmosphere due to ionization and radiative processes. However, protons leave a higher ionization density in the PS compared to muons, approaching the ionization density that could be produced by Dirac MMs within a specific range of speeds. The stopping powers of protons and muons, corresponding to detectable energy ranges, in the PS are calculated based on the PSTAR and ASTAR databases [20], PDG sources [19], and the methodology outlined in Ref. [18]. These stopping powers are presented in Fig.13. To model the flux and angular distribution of atmospheric muons at sea level, the Bugaev/Reyna model [21] is employed, while the flux of high-energy protons is simulated using CRY algorithms [22]. The fluxes can be observed in Fig.15.

On Moon, the muons are no longer dominant because of the absence of atmosphere. In deep space, high-energy protons and helium nuclei emerge as the prevailing particles, as evidenced by findings from the AMS [24, 25], DAMPE [26, 27], and CALET [28, 29] experiments. Assuming the negligible influence of Earth's magnetic field on the Moon, it is conservatively assumed that the fluxes of protons, helium nuclei, carbon nuclei, and iron nuclei are homogeneous in direction. The fluxes as a function of particle kinetic energies are taken from Ref. [23], and are also shown in Fig. 15.

A toy Monte Carlo (MC) simulation is performed to calculate the background and MM spectra. The spread in deposited energy caused by varying travel lengths inside the PS due to different incoming particle angles is also taken into consideration in the toy MC. In the final analysis of the top and bottom PSs, we are able to provide the reconstructed zenith angles of incoming background particles or MMs or the "fake" particles

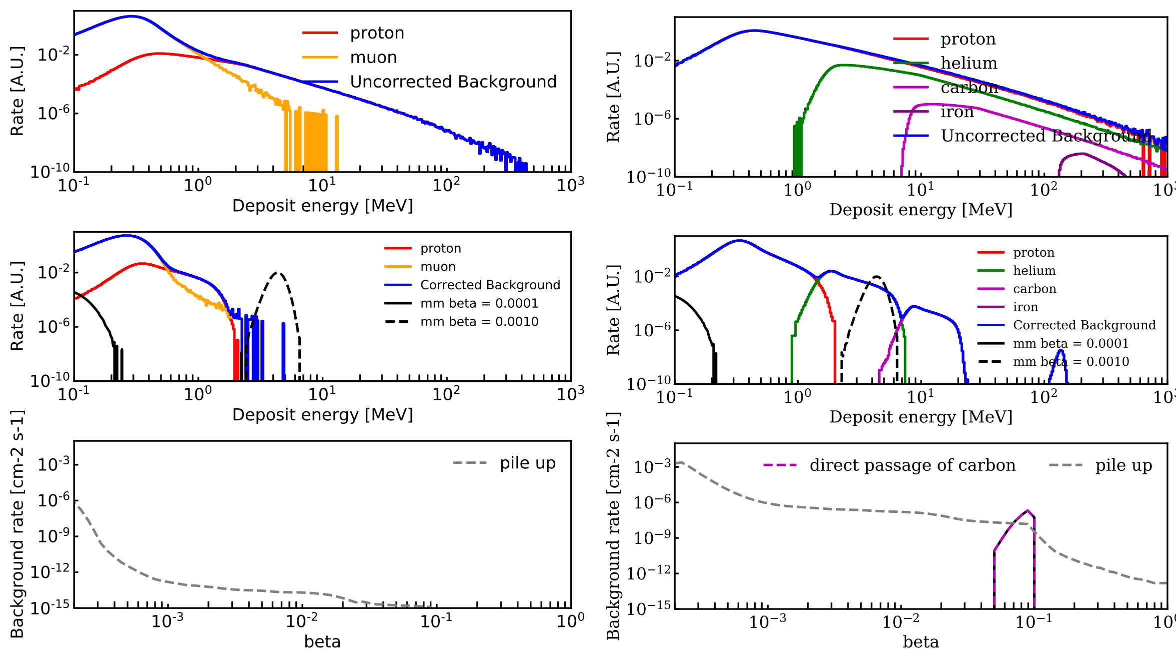

FIG. 16. The simulated reconstructed energy distributions of the background particles and MMs with different speeds from all the angles are shown in the top panels. The middle panels show the energy distribution of background particles and MMs that has been corrected by reconstructed angles. The lower panels show the remaining background rate,including the direct passage component(colored dashed line) and pile up(grey line)component in the, as a function of assumed MM speed. The left and right panels give the results for detectors on Earth and Moon, respectively.

reconstructed from pileups. Therefore, all the deposit energies are corrected to the equivalent deposit energy if it perpendicularly passes through, denoated as E_0. The top panels of Fig.16 illustrates the predicted deposit energy spectra of Dirac MMs and background particles in a single PS (before E_0 conversion). The middle panels give the E_0 differential rates for both the pileup between top and bottom PSs and the direct passage of one particle through the PSs. The lower panels depicts the total scintillation background rate $\mathcal{R}_{PS}$ for different assumed MM speeds, requiring that we select an E_0 range that covers 99.5% (3σ) of MMs and also covers 99.5% (3σ) of MMs' TOFs. Considering the energy threshold of 0.1 MeV in the plastic scintillator, we do not expect its acceptance of MMs with speeds lower than about 2.5×10^{-4} light speed.

D. Total Background and Sensitivity

For high-speed MMs ($\beta > 2\times10^{-4}$),we can detect both their ionization signals and the induction signals. So the final background rate can be calculated by the coincidence between PSs and Coils. Low-speed MMs ($\beta < 2\times10^{-4}$) are unable to produce enough lights to surpass the energy threshold in PS.Such searches need to be performed with induction signal only, and higher number of fired coils is required. So the final background rate can be expressed as:

$$R(\alpha,\beta) = \begin{cases} R_{ind}(\alpha)\cdot R_{ps}(\beta)\cdot \Delta t; & \beta > 2\times10^{-4} \\ \dfrac{R_{ind}(\alpha)}{\pi r_{coil}^2}; & \beta < 2\times10^{-4} \end{cases} \tag{13}$$

Here r_{coil} denotes as the radius of a single coil, and we set it to be 6 cm in the following calculation.The $R_{ind}(\alpha)$ and R_{ps} are given in Subsec. V B and V C, respectively. An optimal α is got by minimizing the value Q shown in the following equation:

$$Q = \frac{\mathcal{FC}(\mathcal{E}\cdot R(\alpha,\beta))}{A_{ps}(\beta)\cdot A_{ind}(\alpha)\cdot\mathcal{E}} \tag{14}$$

Here, $A_{ps}(\beta)$ is the acceptance of PSs, $A_{ind}(\alpha)$ is the acceptance of induction coils from Eq. 10. $\mathcal{E}$ is the assumed exposure. $\mathcal{FC}$ denotes as the Feldman-Cousins upper limit at 90% CI as a function of expected background count, $R(\alpha,\beta)$ is the expected background rate based on Eq. 13. The top and middle panels of Fig. 17 and Fig. 18 show the optimized expected background count and the corresponding acceptance as a function of assumed MMs speed under different SNR_0 and $\mathcal{E}$ assumptions.

With these, we give the estimated sensitivity of MM flux with several assumed detector exposure time and size in the bottom panels of Fig. 17 and Fig. 18. We also plot the most constraints for MM flux at different speed ranges from all the induction experiments [30],

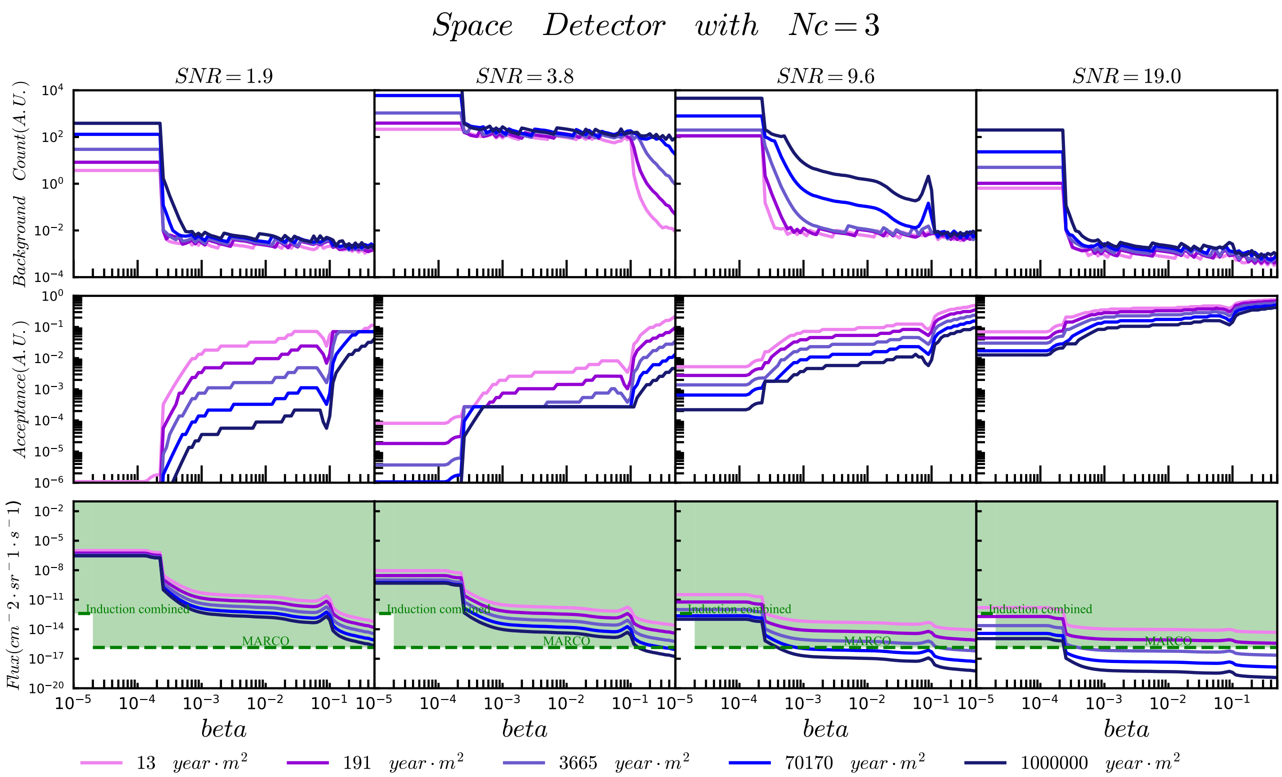

FIG. 17. The proposed sensitivity for a moon-based detector. The top and middle panels show the expected background count and acceptance as a function of assumed MMs speed at an optimized coil's triggering threshold, respectively. The bottom panels illustrate the flux upper limit at 90% CI. The colored solid lines represent the expected constrain that can be obtained from this work, the green region represents the flux constrain that have been get from other works like MARCO and Ice-cube etc. Different colors represent to different exposures, and different columns display the results that are calculated under different SNR_0 assumptions (Need to update)

MACRO [3], and IceCube [31]. SCEP has excellent background suppression for Dirac MMs traveling at speeds exceeding $\sim 2\times10^{-3}$ light speed. This is achieved by exploiting the coincidence between the induction and scintillation signals. Consequently, the sensitivities within this speed range are primarily dominated by the exposure (the product of exposure time and area of detection area). However, when the velocity of the MMs falls within the range of approximately 2.5×10^{-4} to 2×10^{-3}, the scintillation background becomes significant, resulting in a reduction in sensitivity. This effect is particularly noticeable when number of coil layer N_c is equal to 2 and when the detector is based on the Moon. For MMs traveling at speeds below approximately 2.5×10^{-4} light speed, the Dirac MMs are unable to produce scintillation lights in the PSs, causing SCEP to operate solely in induction-only search mode. As a result, sensitivities in this speed range decrease significantly due to the absence of scintillation/induction coincidence. However, the use of a higher number of coil layers can help recover the lost sensitivity. Also, the sensitivity keeps decreasing as the speed of MM decreases due to the SNR's dependence on the MM speed. By employing a simple SCEP benchmark setup consisting of four layers of induction coils, it is anticipated that world-leading sensitivities can be achieved for low-speed MM ($\beta \sim 10^{-5}$) searches with a 500 m^2·yr exposure. Similarly, for medium-to-high-speed MMs ($\beta \sim 10^{-3}$ to 0.7), sensitivities can reach a competitive level with a 200,000 m^2·yr exposure.[need to be update]

VI. SUMMARY AND DISCUSSION

The SCEP experiment aims to detect the induction signal and scintillation signal simultaneously when a MM passes through coils and deposits energy inside PSs. Two read-out scenarios are planned for the induction signal. It can either be directly amplified by an operational amplifier and read out by a digitizer, or the induction micro-current can be fed into a Helmholtz coil, converting it to a magnetic signal that can be read out by a high-precision magnetometer coupled to the Helmholtz coil. The background for the induction signal is primarily influenced by two factors: the backend electronics noise and the thermal noise from the induction coil. In the case of the magnetometer-readout scenario, the backend noise

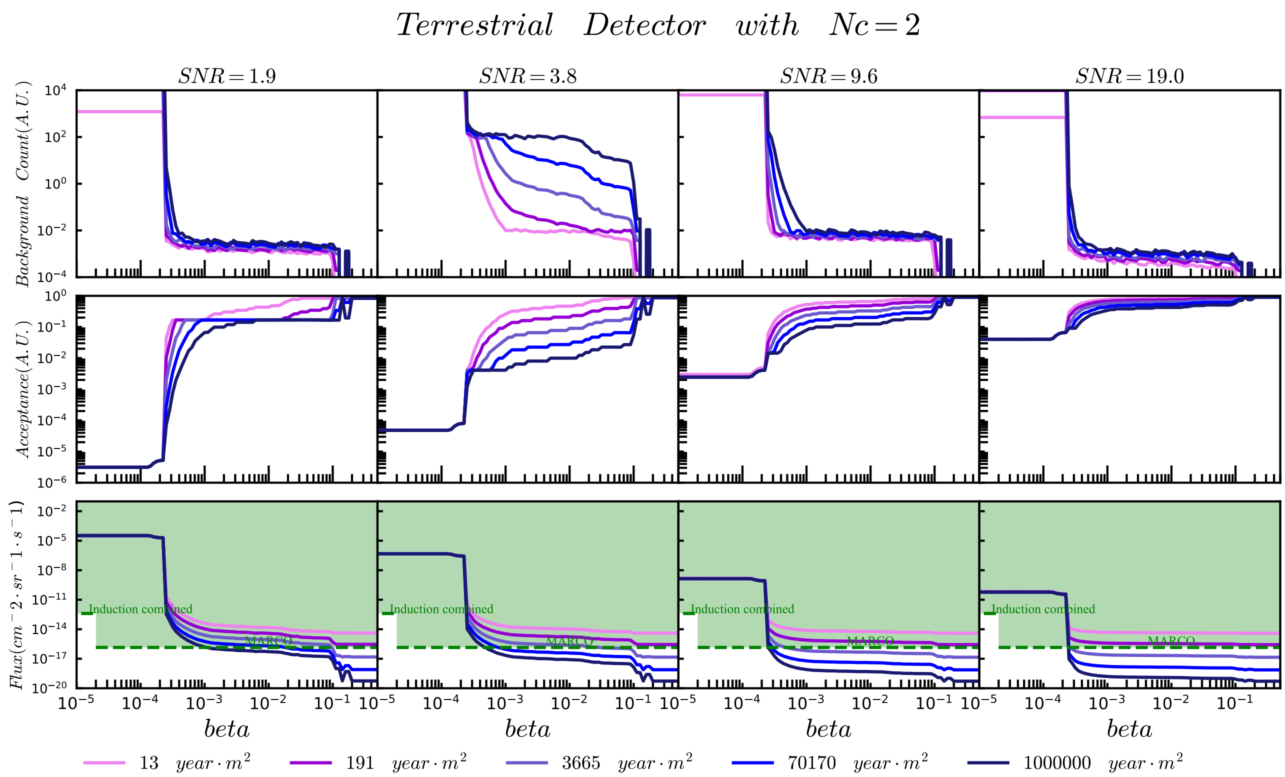

FIG. 18. The proposed sensitivity for a Terrestrial-based detector. The top and middle panels show the expected background count and acceptance as a function of assumed MMs speed at an optimized coil's triggering threshold, respectively. The bottom panels illustrate the flux upper limit at 90% CI. The colored solid lines represent the expected constrain that can be obtained from this work, the green region represents the flux constrain that have been get from other works like MARCO and Ice-cube etc. Different colors represent to different exposures, and different columns display the results that are calculated under different SNR_0 assumptions

is negligible, and the background is dominated by the thermal noise. To estimate the SNR for three prototype induction coils, a dedicated simulation framework has been developed. The results show that the V2 coil with magnetometer readout can achieve an SNR of approximately 2. These findings are further validated through measurements using stimulated pulsed magnetic flux from a long-thin coil and measurements of the thermal noise on the coil. The pileup background for the scintillation signal on the PSs is estimated using dedicated MC simulations, taking into account the particle fluxes at the detector site in both terrestrial (sea-level) and moon-based environments. The pileups are primarily caused by muons and protons for terrestrial detectors, while high-energy protons and helium nuclei dominate in moon-based detectors. By considering all these factors, the sensitivities of the SCEP experiment to Dirac MMs are estimated as a function of MM speed, with different assumed exposures. The simplest benchmark setup, consisting of four layers of induction coils, allows for a background-free search through induction/scintillation coincidence. However, for MMs traveling at speeds below approximately 2.5×10^{-4} light speed, they are unable to produce sufficient scintillation light in the PSs. Consequently, induction-only searches have to be performed in this speed range, and the sensitivity is reduced unless a sufficient number of coil layers are used. With N_c=4 and an exposure of $500\,\mathrm{m}^2{\cdot}\mathrm{yr}$, the SCEP experiment can already achieve the best sensitivity for MM searches at speeds around 10^{-5} light speed.

However, it should be noted that the estimations presented in this work are based on a coil size with a radius of 6 cm. In future large-area detector arrays, there is a preference for larger coil sizes and less number of coil layers due to practical considerations such as reducing the number of readout channels and the total weight of the system. In the ideal case, the SNR on a single coil is proportional to the product of the number of turns, the square of the wire diameter, and the inverse square of the coil diameter, and thus decreases if we simply increase the coil size. This relationship does not even take into account the potential dependence of the alternating resistance on these parameters. On the other hand, increasing the coil size will lead to a decrease in the track reconstruction resolution when using induction signals from multiple coils. Consequently, this can result in a higher background rate after the induction/scintillation coincidence. Therefore, when employing detector arrays with larger coil sizes, it is crucial to optimize the SNR for the induction signal and minimize the background rate of the scintillation signal on the PSs. To improve the SNR of the induction signal, optimization of the induction circuit and the use of materials with high magnetic permeability are two potential approaches. Increasing the number of layers in the particle detectors and incorporating different types of particle detectors hold promise for further reducing the background rate due to particle interactions. Additionally, more advanced algorithms, such as those based on deep neural networks, have the potential to enhance background rejection by leveraging the full range of information obtained from the data.

Taking all of these factors into consideration, it has been demonstrated that SCEP is capable of conducting background-free searches for medium-to-high-speed Dirac magnetic monopoles by requiring the coincidence between the induction and scintillation signals. It is also possible to further increase the SNR of induction searches, allowing for the use of fewer coil layers and increased sensitivity for low-speed magnetic monopoles.

ACKNOWLEDGEMENTS

This project is supported by grants from National Science Foundation of China (No. 12250011), and by the Frontier Scientific Research Program of Deep Space Exploration Laboratory under grant No. 2022-QYKYJH-HXYF-013.

[1] P. A. M. Dirac, Proceedings of the Royal Society of London. Series A, Containing Papers of a Mathematical and Physical Character **133**, 60 (1931).

[2] H. Georgi and S. L. Glashow, Physical Review Letters **32**, 438 (1974).

[3] M. Collaboration and M. Ambrosio, The European Physical Journal C-Particles and Fields **25**, 511 (2002).

[4] R. Abbasi, Y. Abdou, M. Ackermann, J. Adams, J. Aguilar, M. Ahlers, D. Altmann, K. Andeen, J. Auffenberg, X. Bai, *et al.*, Physical Review D **87**, 022001 (2013).

[5] G. Bertone, D. Hooper, and J. Silk, Physics reports **405**, 279 (2005).

[6] D. J. Chung, E. W. Kolb, and A. Riotto, Physical Review D **59**, 023501 (1998).

[7] P. Eberhard, R. Ross, and J. Taylor, Review of Scientific Instruments **46**, 362 (1975).

[8] B. Cabrera, Physical Review Letters **48**, 1378 (1982).

[9] B. ZHOU, X. ZHANG, F. Fang, D. YAN, S. TANG, Y. YU, S. WANG, X. LIU, Y. ZHAO, S. JIN, *et al.*, Nuclear Physics Review **37**, 749 (2020).

[10] S. Agostinelli, J. Allison, K. a. Amako, J. Apostolakis, H. Araujo, P. Arce, M. Asai, D. Axen, S. Banerjee, G. Barrand, *et al.*, Nuclear instruments and methods in physics research section A: Accelerators, Spectrometers, Detectors and Associated Equipment **506**, 250 (2003).

[11] M. Jiang, W. Xu, Q. Li, Z. Wu, D. Suter, and X. Peng, Advanced Quantum Technologies **3**, 2000078 (2020).

[12] M. Jiang, H. Su, A. Garcon, X. Peng, and D. Budker, Nature Physics **17**, 1402 (2021).

[13] The induction coil is connected directly to the amplifier and ADC, but the simulation procedures are mostly identifcal.

[14] S. Somalwar, H. Frisch, and J. Incandela, Physical Review D **37**, 2403 (1988).

[15] J. B. Johnson, Physical Review **32**, 97 (1928).

[16] Note the expression of S_n follows the convension in the field of signal processing [14].

[17] A. V. Oppenheim, *Discrete-time signal processing* (Pearson Education India, 1999) pp. 465–478.

[18] J. Derkaoui, G. Giacomelli, T. Lari, G. Mandrioli, M. Ouchrif, L. Patrizii, and V. Popa, Astroparticle Physics **10**, 339 (1999).

[19] D. E. Groom, N. V. Mokhov, and S. I. Striganov, Atomic Data and Nuclear Data Tables **78**, 183 (2001).

[20] I. C. on Radiation Units and Measurements, *Stopping powers and ranges for protons and alpha particles* (International Commission on Radiation Units and Measurements, 1993).

[21] N. Su, Y. Liu, L. Wang, B. Wu, and J. Cheng, Frontiers in Energy Research **9**, 750159 (2021).

[22] C. Hagmann, D. Lange, and D. Wright, in *2007 IEEE nuclear science symposium conference record*, Vol. 2 (IEEE, 2007) pp. 1143–1146.

[23] J. M. Waller, K. Rojdev, K. Shariff, D. A. Litteken, R. A. Hagen, and A. J. Ross, *Simulated galactic cosmic ray and solar particle event radiation effects on inflatable habitat, composite habitat, space suit and space hatch cover materials*, Tech. Rep. (2020).

[24] M. Aguilar, L. A. Cavasonza, G. Ambrosi, L. Arruda, N. Attig, F. Barao, L. Barrin, A. Bartoloni, S. Başeğmez-du Pree, R. Battiston, *et al.*, Physical review letters **127**, 271102 (2021).

[25] M. Aguilar, L. A. Cavasonza, G. Ambrosi, L. Arruda, N. Attig, F. Barao, L. Barrin, A. Bartoloni, S. Başeğmez-du Pree, R. Battiston, *et al.*, Physical review letters **128**, 231102 (2022).

[26] D. collaboration, Q. An, R. Asfandiyarov, P. Azzarello, P. Bernardini, X. Bi, M. Cai, J. Chang, D. Chen, H. Chen, *et al.*, Science advances **5**, eaax3793 (2019).

[27] D. Collaboration *et al.*, Science Bulletin **67**, 2162 (2022).

[28] P. S. Marrocchesi, N. Cannady, T. Hams, J. F. Krizmanic, K. Sakai, C. Collaboration, *et al.*, (2019).

[29] P. Brogi, K. Kobayashi, O. Adriani, Y. Akaike, K. Asano, Y. Asaoka, E. Berti, G. Bigongiari, W. Binns, M. Bongi, *et al.*, POS PROCEEDINGS OF SCIENCE **395** (2022).

[30] G. Giacomelli, La Rivista del Nuovo Cimento (1978-1999) **7**, 1 (1984).

[31] M. Aartsen, K. Abraham, M. Ackermann, J. Adams, J. Aguilar, M. Ahlers, M. Ahrens, D. Altmann, T. Anderson, I. Ansseau, *et al.*, The European Physical Journal C **76**, 1 (2016).